

Genus Topology of the Cosmic Microwave Background from the WMAP 3-Year Data

J. Richard Gott, III¹, Wesley N. Colley^{2*}, Chan-Gyung Park³, Changbom Park³, and Charles Mugnolo¹

¹*Dept. of Astrophysical Sciences, Princeton University, Peyton Hall, Ivy Lane, Princeton, NJ 08544*

²*Center for Modeling, Simulation and Analysis, D-15 Von Braun Research Hall, Univ. of Alabama in Huntsville, Huntsville, AL 35899*

³*Korea Institute for Advanced Study, 207-43 Cheong-Yang-Ni, Dong-Dae-Mun, Seoul 130-722, Korea*

Accepted . Received

ABSTRACT

We have independently measured the genus topology of the temperature fluctuations in the cosmic microwave background seen in the Wilkinson Microwave Anisotropy Probe (WMAP) 3-year data. A genus analysis of the WMAP data indicates consistency with Gaussian random-phase initial conditions, as predicted by standard inflation. We set 95% confidence limits on non-linearities of $-101 < f_{nl} < 107$. We also find that the observed low ℓ ($\ell \leq 8$) modes show a slight anti-correlation with the Galactic foreground, but not exceeding 95% confidence, and that the topology defined by these modes is consistent with that of a Gaussian random-phase distribution (within 95% confidence).

Key words: cosmology — cosmic microwave background: anisotropy

1 INTRODUCTION

The Wilkinson Anisotropy Probe (WMAP) has revolutionized our understanding of the cosmic microwave background (CMB) anisotropy. In 2003, the team produced its first data release (Bennett et al. 2003a) based on one year of observations. The latest release (Hinshaw et al. 2006) features almost 3 years worth of observations, dramatically increasing the signal-to-noise of the CMB maps.

As with the previous data release, the team has formed best estimates of cosmological parameters based on the data in various combinations with other cosmological information (Spergel et al. 2006), such as Type Ia supernovae (e.g., Riess et al. 2004), elemental abundances predicted by Big Bang nucleosynthesis, and the Hubble Key Project (Freedman et al. 2001), among many others. The tool of choice for assessing these cosmological parameters is the power spectrum of the observed fluctuations in the CMB sky. This is computed by calculating the products of the spherical harmonic coefficients $a_{\ell m}$ and their complex conjugates; then, for each ℓ , those products are summed over all m values to give the total power, C_ℓ , at that angular scale. Different cosmologies predict quite different power-spectra, and so the real data can be tested against predicted power-spectra to give high-confidence estimates of the cosmological parameters.

The $a_{\ell m} a_{\ell m}^*$ product in the power spectrum, however, explicitly removes phase information in the spherical harmonic modes. These phases contain critical information for characterizing the pri-

mordial density fluctuations. Namely, standard inflation (e.g., Guth 1981; Albrecht & Steinhardt 1982; Linde 1982, Linde 1983) predicts that the temperature fluctuations in the CMB, at the resolution measured by WMAP, will be characterized by spherical harmonic coefficients with Gaussian-distributed amplitudes and random complex phases. The WMAP data provide our best opportunity to date to test that hypothesis.

The genus topology method developed by Gott, Melott & Dickinson (1986) directly tests for the Gaussian random-phase nature of a density (or temperature) distribution in 3 dimensions (Adler 1981; Gott, Melott & Dickinson 1986; Hamilton, Gott & Weinberg 1986; Gott, Weinberg & Melott 1987), or in 2 dimensions (Adler 1981; Melott et al. 1989). Coles (1988) independently developed an equivalent statistic in 2 dimensions. The 2 dimensional case has been studied for a variety of cosmological datasets: on redshift slices (Park et al. 1992; Colley 1997; Hoyle, Vogeley & Gott 2002), on sky maps (Gott et al. 1992; Park, Gott, & Choi 2001), and on the CMB, in particular (Gott et al. 1990; Smoot et al. 1992; Kogut 1993; Kogut et al. 1996; Colley, Gott & Park 1996; Park et al. 1998; Park, C-G. et al. 2001). Watts & Coles (2003) and Chiang & Coles (2000), among many others, have investigated other methods for measuring phases, such as looking at the Fourier modes directly.

The WMAP team has carefully measured the genus of the WMAP sky as seen in the new 3-year data (Spergel et al. 2006), and demonstrated that the WMAP results are consistent with the Gaussian random-phase hypothesis. To do this, they carried out a large number of simulations of the CMB, in which the spherical harmonic coefficients were drawn from a Gaussian random-phase

* E-mail: colleyw@uah.edu

distribution. They then used their known beam profiles to synthesize the results in each frequency, and applied the *Kp0* (Hinshaw et al. 2006) mask, just as one would with the real dataset. Using statistical techniques to be discussed at length herein, they determined that the WMAP data are consistent with a Gaussian random-phase field, as predicted by Inflation. They carried out further tests, using other Minkowski functionals (Minkowski 1903; the genus is one functional, others are the area fraction and the contour length) and the bispectrum to verify the Gaussian random-phase hypothesis.

We seek to confirm this result using our own methods. Rather than comparing to simulated Gaussian random-phase realizations of the CMB, we compare data directly to the theoretical prediction for the random-phase genus in two dimensions.

2 WMAP OBSERVATIONS: MAPS

First, we will plot the WMAP data using a color scheme developed by Colley & Gott (2003) and using some new map projections developed by Gott, Mugnolo & Colley (2006) which minimize distance errors.

No map projection of the sphere can be perfect. But projections can conserve some properties. The Mercator Projection is conformal (preserving shapes locally), while the Mollweide projection (an elliptical projection used by the WMAP team) preserves areas.

For conformal projections, Chebyshev (1856) showed the rms local scale errors over a map are minimized when the scale factor on the boundary of the region is a constant (e.g., Snyder 1993). Thus the conformal map of a hemisphere with the smallest rms logarithmic scale errors is the Stereographic projection. The Hammond atlas (1992) has developed optimal conformal projections for individual continents using the Chebyshev criterion of constant scale factor on the boundary. Such a conformal map of the sphere with a boundary cut from pole to pole along the 180° meridian of longitude is the Eisenlohr projection where the scale factor at the boundary is $(3 + 2\sqrt{2})$ times larger than at the center (c.f. Snyder 1993). But this is not necessarily the optimal solution. An eastern and western hemisphere side by side with Stereographic projections would produce a conformal map with a scale factor that varied from the center to the circumference of each hemisphere by a factor of only $\sqrt{2}$. Indeed, by making map projections with more and more interruptions (like the Goode interrupted projection) one can make the scale errors as small as one pleases.

But map projections with many interruptions are unappealing. Why? Boundary cuts can intersect geodesics connecting random points on the globe (Goldberg & Gott 2006). Also, importantly, interruptions take points that are close together on the sphere and put them far apart on the map. The distances between those pairs of points are quite inaccurate. Maps show distances between points and so one also might want to minimize the errors in these distances. This is a global rather than a local criterion and appropriately penalizes projections with too many interruptions. Every map should have a scale bar at the bottom. If two points are shown twice as close on the map as they are on the globe that is just as bad an error as if they were shown twice as far away, so it is the rms logarithmic distance errors between random points on the sphere that we wish to minimize.

Gott, Mugnolo & Colley (2006) have measured the distance errors in different map projections by placing 30,000,000 random pairs of points on the globe and measuring the rms logarithmic distance error between these pairs of points on the map versus the dis-

Figure 1. WMAP three-year data (ILC map) for the celestial sphere using the Gott equal-area elliptical projection with distance errors of 36.5%. The Gott-Colley (2003) color scheme is used. The average temperature is plotted as white. Above average temperatures are plotted in red, with the amount of red ink proportional to the temperature difference from the mean. Below average temperatures are shown in blue, with the amount of blue ink proportional to the temperature difference from the mean. This accurately portrays the symmetry between the hot and cold spots. The galactic center is in the center of the map, the galactic plane is a horizontal line—the major axis of the ellipse. The north galactic pole is at the top of the map, and the south galactic pole is at the bottom. Shapes are shown properly along the central meridian. Since the CMB fluctuations are isotropic, one can see the shape distortions easily as one goes away from the central meridian and toward the edges of the map.

Figure 2. WMAP three-year ILC data, using the Lambert equal-area azimuthal projection, with distance errors of 34.3%. This gives a view of the CMB as reflected in a spherical mirrored garden ball seen from a great distance.

tance between these pairs of points on the globe. (In each case, the overall size of the map relative to the map scale is adjusted to minimize the rms scale error first.) The Mercator projection they find has $\sigma = 0.444$. Thus we may simply say that the Mercator projection has distance errors of 44.4% where the phrase “the rms logarithmic distance error = 0.444 = 44.4% between pairs of random points” is understood. By comparison, the Mollweide projection is better, with distance errors of 39.0%. It avoids the overly large polar areas of the Mercator and plots the north and south poles as points. The Winkel-Tripel projection currently used by the National Geographic Society for its world maps has distance errors of 41.2%. The Hammer equal-area projection has errors of 38.8%.

The new Gott equal-area elliptical projection has distance errors of 36.5% as compared with the Mollweide equal-area projection which has distance errors of 39.0%. The WMAP data are shown in this new projection in Fig. 1. The Mollweide projection has perfect shapes locally at only two points on the central meridian of the map, while the Gott elliptical projection has perfect shapes locally along the entire central meridian. For comparison, the Hammer equal-area projection (with distance errors of 38.8%) has perfect shapes locally only at one point in the center of the map, while the Eckert VI equal-area projection has distance errors of 38.5%, and the sinusoidal equal-area projection has distance errors of 40.7%. Thus, the new Gott equal-area elliptical has smaller distance errors than these other standard projections and has some nice properties in addition. Azimuthal projections offer the possibility of being best overall. The equidistant azimuthal projection has distance errors of 35.6%, and the Lambert equal-area azimuthal projection has distance errors of only 34.3% (see Fig. 2).

The new Gott-Mugnolo azimuthal projection has still smaller distance errors of 34.1%, which is the smallest of all map projections we have studied. Its radial distribution is designed to produce minimal distance errors (see the appendix). We present the WMAP data in this projection in Fig. 3.

Figure 3. WMAP three year data, using the Gott-Mugnolo azimuthal projection with distance errors of 34.1%. We have placed the south galactic pole at the center of the map. The north galactic pole is at the circumference of the map. The galactic equator is a circle centered on the south galactic pole whose radius is 65.4% of the radius of the map.

3 GENUS OF THE WMAP 3-YEAR DATA

The most direct data product from the WMAP team is the “internal linear combination” (ILC) map of the CMB, which is given in the HEALPix format (Górski et al. 2000). This ILC map uses the optimum linear combination of the sky maps at the different frequencies to remove the Galaxy and some other foregrounds (LAMBDA ILC 2006). Note that the method is significantly different than the map used in the 1-year data release (Bennett et al. 2003b), though details of the difference are not perfectly clear. This is the primary map distributed as the best rendering of the CMB and has a resolution (beam width) of $1^\circ \times 1^\circ$. The WMAP team has also produced (as with the 1-year data) a set of masks that can be used to exclude pixels regarded as contaminated by a foreground, Galactic or otherwise. We have chosen the *Kp0* mask provided by the WMAP team.

Colley et al. 2003 describe in detail the computation of the genus on the sphere under a HEALPix map projection. For 2D topology on a plane, the 2D genus of the microwave background is defined as

$$g_{2D} = \text{number of hot spots} - \text{number of cold spots}. \quad (1)$$

For a Gaussian random-phase field,

$$g_{2D} \propto \nu \exp(\nu^2/2), \quad (2)$$

where ν measures the number of standard deviations above the mean temperature (for $\nu > 0$, there are more hot spots than cold spots, and for $\nu < 0$, there are more cold spots than hot spots). The genus is also equal to the integral of the curvature around the temperature contour divided by 2π . If we were to drive a truck around an isolated hot spot, we would have to turn a total angle of 2π as we completed a circuit around the hot spot. Driving a truck around an isolated cold spot, we would turn a total angle of 2π in the opposite sign, with a negative turn angle defined as one that is a turn to the left when the hot region is on your right. This has been carried out on planar images by the program CONTOUR2D which counts the turning observed at each vertex of four pixels in an image (Melott et al. 1989).

We can rigorously define the 2D genus on a spherical surface (Colley et al. 2003). The 2D genus is defined to be equal to minus the 3D genus of solid objects formed by bestowing the hot spots with a small, but finite radial extent. Imagine using lead paint to paint the hot regions onto the surface of a balloon, and after letting the paint dry, bursting the balloon to obtain solid, curved lead shapes that would have a certain 3D genus. Take the minus of this number and that will be g_{2D} , as we will define it.

One hot spot in the north polar region would have a 2D genus of +1 (one hot spot), because the hot spot cap is one isolated region. Suppose the hot region covered all of the sphere except for a cold spot in the south polar region. The genus would still be +1, because this would look like a sugar bowl without any handles, which is also one isolated region in 3D. The topology in each case is identical since one can be deformed into the other. The genus on a plane is determined by the turning that a truck would do driving around the temperature contour surface. Circling a hot spot on a plane would require a total turning of 2π . The Gaussian random-phase formula measures this local turning. Circling a hot spot on the sphere involves a total turning of $2\pi - 4\pi f$, where f is the fraction of the sphere in the hot spot (because the deficit produced by parallel transport on the sphere is equal to the enclosed area). Dividing by 2π , we may define the effective genus:

$$g_{2D,eff} = g_{2D} - 2f, \quad (3)$$

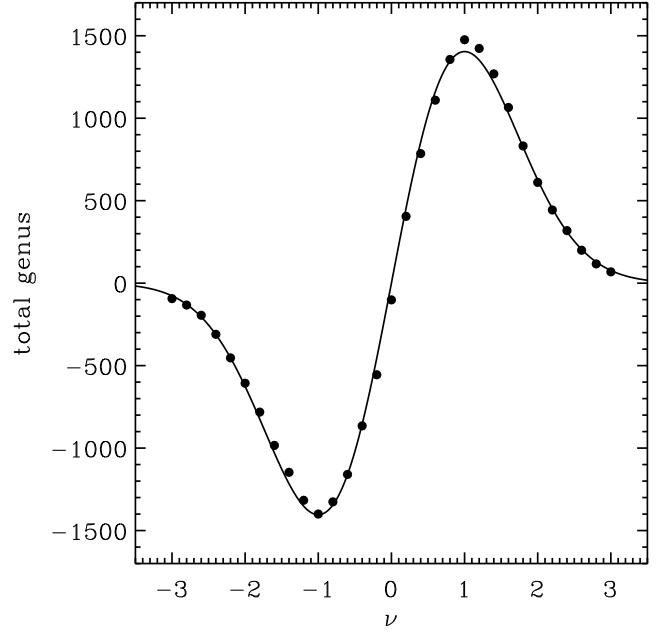


Figure 4. Total genus, $g_{2D,eff}$, in the WMAP 3-yr ILC (internal linear combination), which is smoothed to a FWHM of 1 degree. HEALPix pixels excluded by the suggested *Kp0* mask have been omitted in the genus computation. The solid curve shows the best-fit random-phase curve $g(\nu) \propto \nu \exp(-\nu^2/2)$.

where f is the fraction of the area of the sphere in the hot spots. For a Gaussian random-phase field on the sphere

$$g_{2D,eff} \propto \nu \exp(-\nu^2/2), \quad (4)$$

because the Gaussian random-phase field behaves locally on the sphere just as it does on the plane to produce this particular contribution to the turning integral. Thus, in comparing the WMAP data to the random-phase formula, we will use $g_{2D,eff}$, as defined rigorously above.

We have implemented this method on the HEALPix map projection as follows. Within any of the 12 principal diamonds on the projection, the method is as straightforward as on any planar image. However, much care must be taken where diamonds meet so as not to overcount or undercount any pixel vertices. Also, in 8 places on the sphere, three diamonds meet at a single vertex (such corners contain all of the curvature in the projection); these special vertices are addressed carefully in Colley et al. 2003. Masking a portion of the sphere means the contours around various structures may be cut off randomly by the mask. However, this randomness is what we rely on. Colley et al. 2003 show that as long as the mask does not preferentially excise higher or lower temperature pixels than average, the genus will be, on average, unaffected, although the number of structures will be expected to decline by a fraction equal to the fraction of the total sphere excised by the mask.

Fig. 4 shows the total genus of the masked WMAP 3-year data. We do not provide errorbars (most are so small they would be inside the plot points anyway), because, as we will soon show, simple independent errorbars are not sufficient to convey the information on the quality of fit to the curve.

Colley (1997) introduced a new method for computing the confidence of fit for the 2-D genus curve. In that work, the genus of the galaxy distribution as observed in the Las Campanas Redshift Survey (Schechtman et al. 1996) was computed. To characterize

the quality of fit of the LCRS genus to the 2-D theoretical genus curve, the author created 100 fake 2-D random-phase fields with a power-spectrum of $n = -1$, then cut out of those maps fan shapes that matched the fanned shapes of the 6 redshift slices in the LCRS. With these 100 fake density maps, one could perform genus computations on each, and, as with the real data, find the best-fit Gaussian random-phase genus curve. The errors with respect to that curve, at each value of ν can be cross-correlated to give a covariance matrix $C(\nu_1, \nu_2)$ which contains the expected product of the errors in the genus at ν_1 and ν_2 . Very similar analysis was carried out for the IRAS 1.2-Jansky Redshift Survey by Protogeros & Weinberg (1997) nearly coincidentally with Colley's work.

Spergel et al. 2006 carry out a very similar calculation in their analysis of the genus. One very important distinction is that those authors compare their genus values directly to the means measured in their fake maps. Based on the best-fit flat-lambda model, they find that the WMAP data produce a genus curve that looks excellent but has a high amplitude compared to the mean genus of the fake maps. The amplitude of the genus curve depends only on the shape of the power spectrum, so the errors they found are primarily due to errors in the power spectrum (if nothing else, the quadrupole is low relative to that predicted by the best-fit flat-lambda model, predicting a genus amplitude that is too high), rather than errors in the random-phase nature of the temperature distribution. Because the amplitude is a function only of the power-spectrum, which we are not interested in here, we do not impose an amplitude constraint.

We carry out an alternate analysis herein. First, we created 200 maps of fake CMB signal with the same power spectrum as that measured by the WMAP team for the 3-year data release (Spergel et al. 2006). We computed the genus, just as we did in Fig. 4 for all 200 maps. In this case, we simply took the mean genus at the 31 ν values from all 200 maps and evaluated the errors in each map with respect to that mean. Again, multiplying the error at ν_1 by the error at ν_2 gives the covariance $C(\nu_1, \nu_2)_j$ for each map j . Averaging this matrix over the 200 maps gives us an excellent estimate of the covariance matrix, $C(\nu_1, \nu_2)$ with which to carry out confidence of fit computations.

As did Spergel et al. (2006), we observe that the genus amplitude in our fake maps is not as high as in the real WMAP data. Since the amplitude is a function only of the power-spectrum, there are two possible sources of this discrepancy: mis-estimation of the power-spectrum, and noise in the real data. We are only using the fake maps to produce a reasonable characterization of the errors (covariance matrix), so we need only concern ourselves with how well genus deviations in the fake maps correspond to the expected deviations in the real data. To investigate this issue, we have carried out a great many Monte Carlo experiments using synthetic Gaussian random-phase maps with various power-spectra to estimate the effect on the covariance matrix when small changes in the power-spectrum and pixel noise are introduced. To very good approximation, the only effect is to multiply the original covariance matrix by a factor equal to ratio of the new amplitude to the original amplitude. Specifically, the greatest change to any element of the covariance matrix, other than this ratio, is typically of the order of the fractional difference of the ratio and 1—if the amplitude increases by 10%, then the worst discrepancy of a single covariance matrix element from the original covariance multiplied by 1.1, is of order 10%. Most of the elements, in fact, do much better. We therefore regard our best estimate of the covariance matrix for the WMAP data as the covariance determined from the 200 fake CMB maps, multiplied by the ratio of the amplitude of the real data vs. the mean amplitude from the fake maps. The resulting covariance matrix is

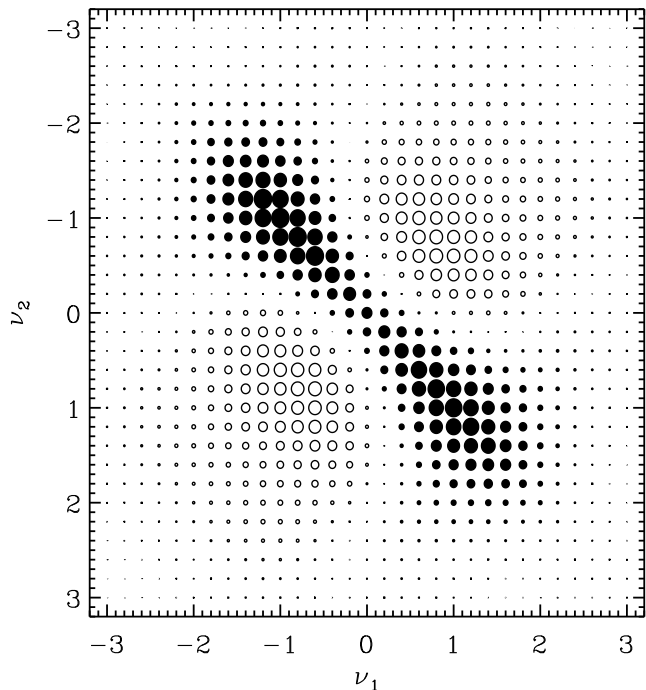


Figure 5. Covariance matrix of the genus measured at different values of ν , as derived from the 200 simulated CMB datasets. Covariance is proportional to symbol size, and negative covariances are shown as open symbols.

illustrated in Fig. 5 (following Protogeros & Weinberg 1997). The size of the circles is proportional to the covariance; filled circles indicate positive covariance, and open circles indicate negative covariance.

Before using this covariance matrix to carry out goodness of fit calculations, we shall first examine how necessary it is to go to such lengths. We can force the covariance matrix to be diagonal by disregarding the off-diagonal terms, and inserting along the diagonal, the squares of the direct one-sigma errorbars observed at each genus point among the 200 fake maps. Computing the best fit amplitude for each map, and the corresponding χ^2 in the “usual” way used for independent datapoints yields Fig. 6. The histogram of the χ^2 values are shown in outline. Overplotted is the expected distribution of 200 χ^2 values for 30 degrees of freedom (31 minus the amplitude fit). Obviously, the performance is terrible (because the individual data points are not independent). Plotted as a solid box is the WMAP data (whose errorbars have been scaled by the square-root of the amplitude ratio, as discussed above). The WMAP genus, according to this ostensibly inept statistic, acquires a naively good value of $\chi^2 = 18.0$, but this is actually just so-so with respect to the χ^2 values from the fake maps, coming in at a rank of 142nd out of the 201 total maps (200 fake maps + 1 real map).

After that aside, we carry on with the full covariance treatment of the WMAP genus. First, we find the best fit amplitude by minimization of χ^2 as usual. For a full covariance matrix, C , the best fit amplitude is given as

$$A_{\text{best}} = \frac{\vec{g} \cdot C^{-1} \vec{g}_{2D}}{\vec{g}_{2D} \cdot C^{-1} \vec{g}_{2D}}, \quad (5)$$

where \vec{g} is the vector of measured genus values over the selected ν values, and $g_{2D,i} = \nu_i \exp(-\nu_i^2/2)$, the analytic form of the Gaussian random-phase two-dimensional genus curve for the same ν_i values—note that this formula would be slightly more compli-

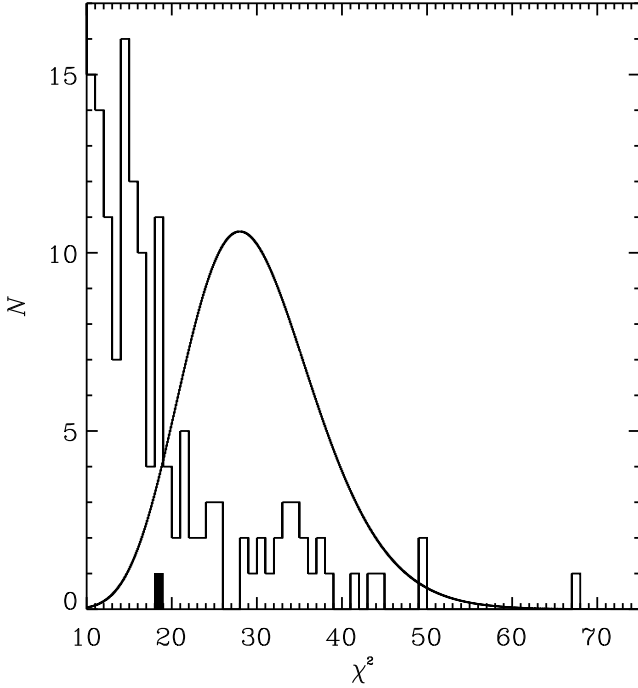


Figure 6. Histogram of χ^2 values for genus derived from the 200 simulated CMB datasets (line), and for the genus derived from the real WMAP data (solid box). χ^2 values are computed assuming a diagonal-only covariance matrix (i.e., errors are regarded as independent among the ν -values).

cated were C not symmetric. χ^2 is computed in full covariance matrix form as follows,

$$\chi^2 = [\vec{g} - A_{\text{best}} \vec{g}_{2D}] \cdot C^{-1} [\vec{g} - A_{\text{best}} \vec{g}_{2D}]. \quad (6)$$

Fig. 7, as with Fig. 6 shows the histogram of χ^2 values for the 200 fake maps in outline, and the expected distribution of 200 χ^2 variates with 30 degrees of freedom as the solid curve. Notice that the χ^2 values fit the expected distribution much, much better than in Fig. 6. The solid block in Fig. 7 gives the locus of the WMAP χ^2 value of 27.38. The cumulative probability that a 30 d.o.f. χ^2 variate would exceed this value is 60%, while the rank of the WMAP data among the 201 total maps is 73rd, both excellent confirmations of the Gaussian random-phase hypothesis.

4 NON-LINEARITY

Various theories for non-linear perturbations in the CMB temperature maps can be approximated as a simple 2nd-order correction to the linear theory (Spergel et al. 2006). On the scales we are considering (i.e., a smoothing length of 1°), the Sachs-Wolfe (1967) effect is dominant, so

$$\frac{\Delta T}{T} = -\frac{1}{3}\Phi, \quad (7)$$

where Φ is the curvature perturbation. If we were considering smaller smoothing scales, velocity effects would have to be considered and on much larger scales, the integrated Sachs-Wolfe effect would have to be considered. Following Spergel et al. (2006),

$$\frac{\Delta T}{T} = -\frac{1}{3}\Phi(\vec{x}) = -\frac{1}{3}[\psi(\vec{x}) + f_{nl}\psi^2(\vec{x})], \quad (8)$$

where $\psi(\vec{x})$ is a Gaussian random-phase field that is simply a scaled version of the unit Gaussian random-phase field $\nu(\vec{x})$:

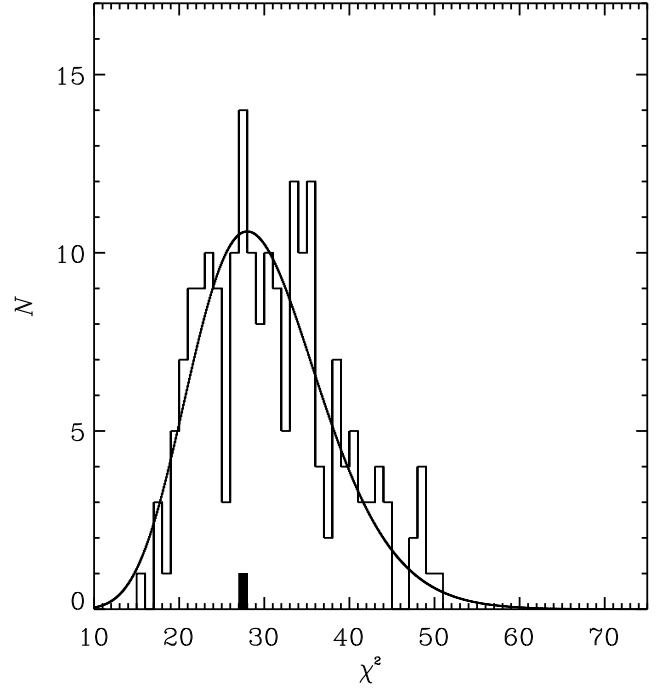


Figure 7. As Fig. 6, except that the full covariance matrix (see Fig. 5) is used to compute the values of χ^2 .

$\psi(\vec{x}) = -\sigma_\psi \nu(\vec{x})$, and f_{nl} is the amplitude of the non-linear effects. The temperature map in the CMB is thus given by

$$\frac{\Delta T}{T} = -\frac{1}{3}\Phi = \frac{1}{3}(\sigma_\psi \nu - f_{nl} \sigma_\psi^2 \nu^2). \quad (9)$$

Of course, the quadratic term will shift the observed mean and change the standard deviation.

$$\begin{aligned} \left\langle \frac{\Delta T}{T} \right\rangle &= -\frac{1}{3} f_{nl} \sigma_\psi^2 \\ \left\langle \left(\frac{\Delta T}{T} \right)^2 \right\rangle &= \frac{1}{9} \sigma_\psi^2 + \frac{1}{3} f_{nl}^2 \sigma_\psi^4, \end{aligned} \quad (10)$$

the second of which can be used to compute the true standard deviation in ψ ($=\sigma_\psi$) from the observed standard deviation in temperature and f_{nl} .

When computing the genus in the usual way (subtract the mean and normalize by standard deviation), one would observe

$$\nu_{obs} = \frac{\frac{\Delta T}{T} - \left\langle \frac{\Delta T}{T} \right\rangle}{\left\langle \left(\frac{\Delta T}{T} \right)^2 \right\rangle^{1/2}} = \frac{\frac{1}{3}(\sigma_\psi \nu - f_{nl} \sigma_\psi^2 \nu^2) + \frac{1}{3} f_{nl} \sigma_\psi^2}{\sqrt{\frac{1}{9} \sigma_\psi^2 + \frac{1}{3} f_{nl}^2 \sigma_\psi^4}} \quad (11)$$

Inversion of this equation allows us to compute the true value of ν from an observed ν_{obs} : $\nu = \nu(\nu_{obs}, f_{nl}, \sigma_\psi)$, which can be used in the usual 2D random-phase genus formula, $g(\nu) \propto \nu \exp(-\nu^2/2)$.

The form of the analytic genus-curve, of course, changes under this transformation, and so one can test the measured genus against the non-linear genus curve by again using the χ^2 test. Fig. 8 shows the value of χ^2 as a function of f_{nl} . Overplotted is the horizontal line at which the value of χ^2 is excluded at 95% confidence for 30 degrees of freedom. We find the f_{nl} is bounded to range between -101 and $+107$ to maintain consistency with the observed genus curve at the 95% confidence level. Notice that the minimum of the χ^2 curve occurs very close to $f_{nl} = 0$ which corresponds to the true random-phase distribution with no non-linear effects.

Fig. 9 shows how discrepant the non-linear genus curves are from the observed genus values. In red, we have $f_{nl} = -101$,

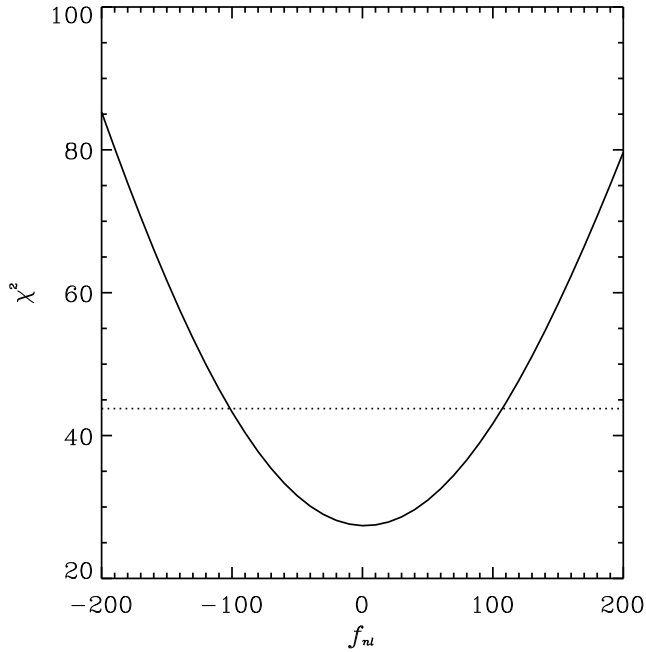


Figure 8. χ^2 as a function of f_{nl} . The horizontal line indicates the 95% confidence interval for a χ^2 variable with 30 degrees of freedom.

and in blue $f_{nl} = +107$. In both cases, the best-fit amplitude has decreased compared to the best-fit for the linear genus curve. This is not surprising—when a less appropriate function is fit in amplitude to a set of points, the amplitude is usually reduced.

Most of the power of this χ^2 test for non-linearity lies not in the peaks, where the amplitude change is most noticeable, but in the wings of the genus curve. Two factors are at work. First, the covariance matrix has very small entries for high and low ν (see Fig. 5), which makes any departure from the normal genus curve more difficult there. Second, most of the non-linear “action” is in the wings. These two factors introduce sufficient statistical power to allow the apparently slight departures from the Gaussian random-phase curve in Fig. 9 to be rejected with 95% confidence.

Our results are similar to those obtained for the WMAP one-year data, $-54 \leq f_{nl} \leq 134$ (Komatsu et al. 2003 in Spergel et al. 2006) at the 95% confidence level. Both support standard inflation which predicts f_{nl} of order unity due primarily to non-linear gravitational effects at recombination; the contribution from slow-roll inflation is much less, of order 0.01 (e.g., Komatsu & Spergel 2000; Maldacena 2005 and references therein).

5 LOW ℓ MODES

The low ℓ power-spectrum of the CMB produced by WMAP has generated substantial interest due to some fairly surprising behaviors. The quadrupole moment appears to be strangely low, we have noticed that the next several moments appear to oscillate in sawtooth fashion about the best-fit flat-lambda power-spectrum. This behavior reminds one of “ringing” in Fourier space of a real feature in the sky with a negative quadrupole moment. Of course, the Galaxy produces a large positive quadrupole, which must be very carefully subtracted off to reveal the CMB behind it. Could it be that the Galaxy has been over-subtracted, causing a small quadrupole (and associated ringing) in the low ℓ modes of the power-spectrum? (e.g., Park et al. 2006)

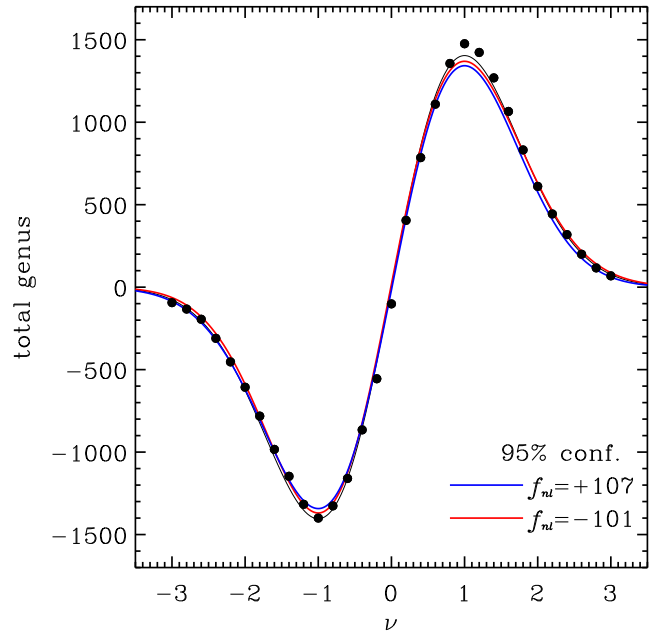


Figure 9. The genus curves for $f_{nl} = 0$ in black, for $f_{nl} = -101$ in red, and $f_{nl} = +107$ in blue. The latter two of these represent the boundaries of 95% confidence interval for f_{nl} as shown in Fig. 8.

First, we simply look at the modes themselves, in real-space on the sky. Fig. 10 (top) shows the first 8 modes of the foreground given by the WMAP team. The galaxy is obvious, as is ringing at a galactic latitude of roughly 45° . Next, we look at the first 8 modes of a foreground cleaned map (Park et al. 2006) in Fig. 10 (bottom). On first blush, the two maps show little correspondence; however, a closer inspection reveals some apparent anti-correlations. Notice that the largest cold (blue) spot in the cleaned map lies on the galactic plane, while the largest hot (red) spot in the cleaned map (on the left) lies on the coldest point of the galactic plane. Also, there is some possible mischief at the $\pm 45^\circ$ bands in the cleaned map, which corresponds to the ringing in the foreground map.

To test whether these coincidences would have occurred randomly, we conducted a correlation analysis. First, we constructed 200 fake maps with $\ell \leq 8$, and correlated these with the foreground map, by simply adding up the product of the pixel values from each map,

$$R = \sum_i^{\text{all pix}} \Delta T_i(\text{foreground}) \cdot \Delta T_i(\text{map}). \quad (12)$$

Fig. 11 shows as a solid histogram the correlation sums for the 200 fake maps correlated with the real foreground. Overplotted is a Gaussian with the standard deviation and mean of the distribution of the correlations. The same figure shows as a solid block and heavy vertical line at -0.65 on the graph, the anti-correlation of the cleaned map. This anti-correlation is rare at the -1.35σ level ($P = 8.9\%$), i.e., 91.1% of random maps would be less anti-correlated. The value ranks 17 out of the 201 total datasets analyzed, so 184 out of 201 are less anti-correlated. While this is a confirmation of what we see with our eyes, the value falls well short of the two-sided 2σ threshold ($P = 2.275\%$), so we do not regard this anti-correlation as statistically significant. We further tested the correlation by rotating the cleaned map by 90° , such that the origin of galactic coordinates ($\ell_{\text{II}} = 0^\circ, b_{\text{II}} = 0^\circ$) is placed at the north pole, and re-ran the correlation. Here, we find a positive correlation

Figure 10. Mollweide projection of the WMAP foreground (blue = -0.4mK , red = $+0.4\text{mK}$) [top], and of the SILC cleaned map (blue = -0.08mK , red = $+0.08\text{mK}$) [bottom].

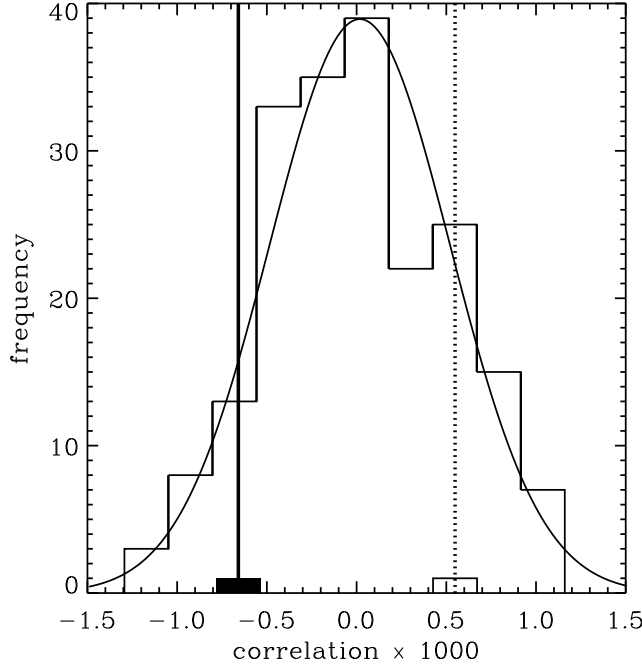


Figure 11. Correlations of a set of 200 fake $\ell \leq 8$ maps with the WMAP foreground $\ell \leq 8$ map (line histogram). Shown as the black box and heavy vertical line on the left is the locus of the correlation of the cleaned ILC map at $\ell \leq 8$. This reveals some anti-correlation. The open box and dotted vertical line on the right show the locus of the correlation of the same map, rotated 90° .

of 0.584 (shown on Fig. 11 as an open box and dotted vertical line). This occurs at the $1.06\text{-}\sigma$ interval ($P = 85.3\%$), and is therefore also consistent with the distribution of fake map correlations. A separate, detailed analysis of foregrounds, masks and correlations with the foregrounds in the low- ℓ modes has been carried out by Oliveira-Costa & Tegmark (2006). These authors confirm the notion that errors in the low- ℓ modes are largely due to foregrounds.

As a final test, we have measured the genus of the $\ell \leq 8$ cleaned map. Because there are few structures, we only test in the range $-2 < \nu < 2$. Whenever a low number of modes is encountered, as in this case, it is essential to use Eq. 3 rigorously to account for the curvature of the sphere. Fig. 12 shows the actual genus of the $\ell \leq 8$ cleaned map as solid points, with the best-fit analytic curve overplotted. For statistical comparison, we used the same 200 fake $\ell \leq 8$ maps from above and measured their genus values in the same range. As we did with the 1-degree maps, we constructed from these 200 maps the covariance matrix of the genus values, so that we could measure χ^2 formally for the real data. Fig. 13 shows the histogram of the χ^2 values for the 200 fake maps, and the overplotted χ^2 distribution for 20 degrees of freedom. The cleaned map produces a χ^2 value of 27.8 (shown on the figure as a black box), which occurs at $P = 88.5\%$, again well inside the 95% ($2\text{-}\sigma$) limit. The value ranks 178 out of the 201 datasets tested. Both of these tests, therefore, show that the low- ℓ modes observed by WMAP are consistent with the Gaussian random-phase hypothesis.

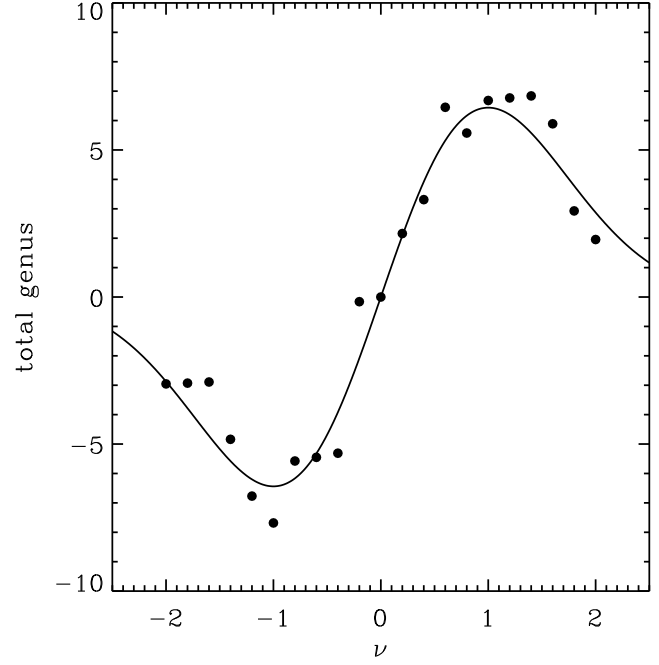


Figure 12. Genus, $g_{2D,eff}$, of the $\ell \leq 8$ map, with the analytical random-phase genus curve after a best-fit for amplitude has been made.

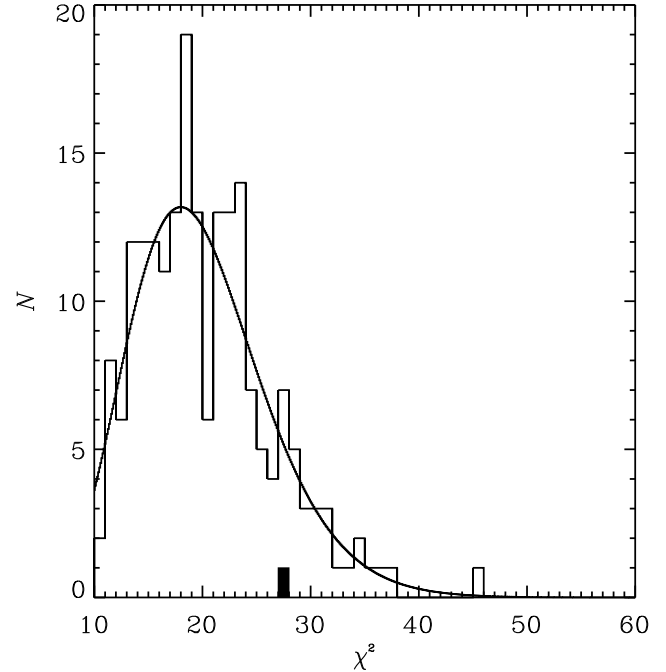


Figure 13. Histogram of χ^2 values for fits of the analytical genus curve to the 200 fake $\ell \leq 8$ maps (solid line) and for the cleaned ILC map (solid box).

ACKNOWLEDGMENTS

The WMAP datasets were developed by Princeton University and NASA's Goddard Space Flight Center, and graciously provided to the public at <http://lambda.gsfc.nasa.gov/>. JRG thanks the National Science Foundation for support under grant AST04-06713. WNC would like to thank NASA and the Center of Modeling, Simula-

tion and Analysis for providing computational services and indirect support for some of this work. CBP acknowledges the support of the Korea Science and Engineering Foundation (KOSEF) through the Astrophysical Research Center for the Structure and Evolution of the Cosmos (ARCSEC), and through the grant R01-2004-000-10520-0.

REFERENCES

- Adler, R. J., 1981, *The Geometry of Random Fields*, Wiley, New York
- Albrecht, A., & Steinhardt, P., 1982, *Phys. Rev. Letters*, 48, 1220
- Bennett, C. L., Halpern, M. et al., 2003a, *ApJS*, 148, 1
- Bennett, C. L., Hill, R. S., et al., 2003b, *ApJS*, 148, 97
- Chebyshev, P. L. (1856) *Bulletin de l'Academie Imperiale des Sciences [St. Petersburg]*, Classe Physico-Mathematique 14, 257.
- Chiang, L.-Y., Coles, P., 2000, *MNRAS*, 311, 809
- Coles, P., 1988, *MNRAS*, 234, 509
- Coles, P., & Plionis, M., 1991, *MNRAS*, 250, 75
- Colley, W. N., 1997, *ApJ*, 489, 471
- Colley, W. N. & Gott, J. R. 2003, *MNRAS*, 344, 686
- Colley, W. N., Gott, J. R., Park, C., 1996, *MNRAS*, 281, 4, L84
- Freedman, W. J., et al. 2001, *ApJ*, 553, 47
- Geocart Version 2.6, the Macintosh map projection program, <http://www.mac-maps.com> (May 2, 2005)
- Goldberg, D., & Gott, J. R., 2006, *Cartographica*, submitted, astro-ph/0608501
- Górski, K. M., Hivon, E., Stompor, R., Banday, A. J., & Bartelmann, M., 2000, *HEALPix website*, URL: <http://www.eso.org/science/healpix/>
- Gott, J. R., et al., 1990, *ApJ*, 352, 1
- Gott, J. R., Mao, S., Park, C., Lahav, 1992 *ApJ*, 385, 26
- Gott, J. R., Melott, A., Dickinson, M., 1986, *ApJ*, 306, 341
- Gott, J. R., Mugnolo, C., & Colley, W. N., 2006, *Cartographica*, submitted, astro-ph/0608500
- Gott, J. R., Weinberg, D., Melott, A., 1987, *ApJ*, 319, 1
- Guth, A. 1981, *Phys. Rev. D*, 23, 347
- Hamilton, A. J. S., Gott, J. R., Weinberg, D. H., 1986, *ApJ*, 309, 1
- Hammond Atlas of the World, 1992, Hammond Incorporated, Maplewood, NJ.
- Hinshaw, G., Nolta, M. R., Bennett, C. L., Bean, R., Doré O., Greason, M. R., Halpern, M., Hill, R. S., Jarosik, N., Kogut, A., Komatsu, E., Limon, M., Odegard, N., Meyer, S. S., Page, L., Peiris, H. V., Spergel, D. N., Tucker, G. S., Verde, L., Weiland, J. L., Wollack, E., & Wright, E. L., 2006, (submitted)
- Hoyle, F., Vogeley, M. S., Gott, J. R., 1, 2002, *ApJ*, 570, 44
- Komatsu, E., et al., 2003, *ApJS*, 148, 119
- Kogut, A., 1993, *BAAS*, 183, 121.03
- Kogut, A., Banday, A. J., Bennett, C. L., Gorski, K. M., Hinshaw, G., Smoot, G. F., Wright, E. L., 1996, *ApJ*, 464, 29
- LAMBDA ILC (Legacy Archive for Microwave Background Data Analysis—Internal Linear Combination Map), 2006, http://lambda.gsfc.nasa.gov/product/map/dr2/ilc_map_info.cfm
- Komatsu, E., et al. 2003, *ApJS*, 148, 119
- Komatsu, E., & Spergel, D. N., 2000, astro-ph/0012197
- Linde, A., 1982, *Physics Letters*, 108B, 389
- Linde, A., 1983, *Physics Letters*, 129B, 177
- Maldacena, J., 2002, astro-ph/0210603v5
- Melott, A., Cohen, A. P., Hamilton, A. J. S., Gott, J. R., Weinberg, D. H., 1989, *ApJ*, 345, 618
- ness, A. G., et al., 2004, *ApJ*, 607, 665
- Minkowski, 1903, *Mathematical Annalen*, 57, 447
- Oliveira-Costa, A., & Tegmark, M., 2006, astro-ph/0603369
- Park, C., Colley, W. N., Gott, J. R., Ratra, B., Spergel, D. N., Sugiyama, N., 1998, *ApJ*, 506, 473
- Park, C., Gott J. R., Choi, Y. S., 2001, *ApJ* 553, 33
- Park, C., Gott J. R., Melott, A., Karachentsev, C. H., 1992, *ApJ*, 387, 1
- Park, C-G., Park, C., Ratra, B., Tegmark, M., 2001, *ApJ*, 556, 582
- Park, C-G., Park, C., Gott, J. R., 2006, *ApJ*, submitted, astro-ph/0608129
- Protogeros, A. M., & Weinberg, D. H., 1997, *ApJ*, 489, 457
- Sachs, R. K., & Wolfe, A.
- Schectman, S. A., Landy, S. D., Oemler, A., Tucker, D. L., Lin, H., Kirshner, R. P., & Schechter, P. L., 1996, *ApJ*, 470, 172
- Smoot, G., et al., 1992, *ApJ*, 396, L1
- Snyder, J. P. (1993), *Flattening the Earth*, University of Chicago Press, Chicago.
- Spergel, D. N., Bean, R., Doré, O., Nolta, M. R., Bennett, C. L., Hinshaw, G., Jarosik, N., Komatsu, E., Page, L., Peiris, H. V., Verde, L., Barnes, Halpern, C. M., Hill, R. S., Kogut, A., Limon, M., Meyer, S. S., Odegard, N., Tucker, G. S., Weiland, J. L., Wollack, E., & Wright, E. L., 2006 (submitted)
- Watts, P., & Coles, P., 2003, *MNRAS*, 338, 806

APPENDIX A: NEW MAP PROJECTIONS

The new Gott equal-area elliptical projection, designed by JRG to lessen distance errors, is produced in the following way: Collapse the longitudes by a factor of two toward the central meridian so the whole globe is mapped onto one hemisphere of the globe. Now establish east and west “poles” 180° apart on the equator, at the eastern and western edges of this hemisphere, and define “new longitude and latitude” relative to these two poles. Then collapse the “new longitudes” by a factor of two (toward the equator) so that the whole globe is mapped onto a quadrant of the sphere. The north pole is now plotted at longitude 0° and latitude $+45^\circ$, while the south pole is plotted at longitude 0° and latitude -45° . Both the first compression in longitude and the second compression in “new longitude” preserve relative areas, so the combination does as well. Then map this quadrant of the sphere onto a plane with a transverse equal-area Bromley-Mollweide projection. (The Bromley-Mollweide projection is like the Mollweide projection-elliptical, with elliptical longitude lines and straight latitude lines, but stretched to produce an ellipse with an axis ratio of $\pi^2/4 : 1$ so that the equator becomes a standard parallel where shapes are preserved locally). Since the quadrant being mapped is bounded by two lines of “new longitude” and such lines are plotted as ellipses by the transverse Bromley-Mollweide projection, the Gott projection will map the earth onto an ellipse. Since the longitude and “new longitude” compressions are by a factor of two each in the horizontal and vertical directions along the central meridian in the map and the transverse Bromley-Mollweide projection preserves shapes along this line, the Gott projection will preserve shapes locally along the central meridian. The map is an attractive ellipse with an axis ratio of $16/\pi^2 : 1$ or $1.62211 : 1$, close to the golden mean (which is $[1 + \sqrt{5}]/2 : 1$ or 1.618). The formulas for the Gott equal-area elliptical projection are as follows. Cartesian map coordinates (x, y) may be calculated from the latitude and longitude (ϕ, λ) (in radians) of a point on the globe by first defining a “new latitude” and “new longitude”:

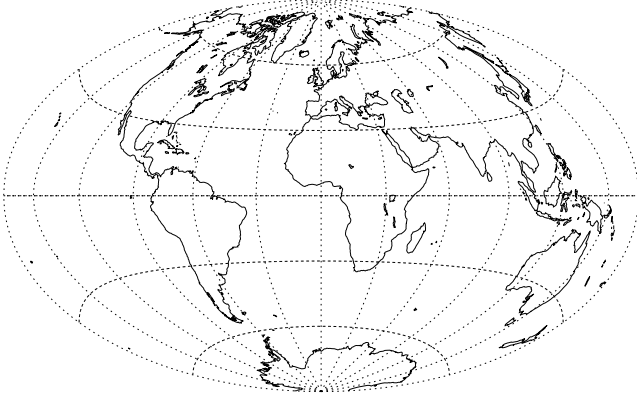


Figure A1. Map of the Earth using the Gott equal-area elliptical projection. Local shapes are perfect along the Greenwich Meridian

Figure A2. Map of the Mars using the Gott equal-area elliptical projection. Local shapes are perfect along the central meridian. Original imaging data from NASA/USGS (Viking Spacecraft).

$$\begin{aligned}\phi' &= -\arcsin[\cos \phi \cdot \sin(\lambda/2)] \\ \lambda' &= 0.5 \arcsin(\sin \phi / \cos \phi')\end{aligned}\quad (\text{A1})$$

Then,

$$\begin{aligned}2\theta + \sin 2\theta &= \pi \sin \phi' \\ x &= -\sqrt{2} \sin \theta \\ y &= \frac{\pi}{2\sqrt{2}} \lambda' \cos \theta\end{aligned}\quad (\text{A2})$$

In Fig. A1 we have shown a map of the earth using this new Gott equal-area elliptical projection. Shapes are preserved locally along the central meridian. The distance scale is also linear along this meridian. This has good shapes for Europe, Africa, and Antarctica. The polar areas are better displayed than in the Mollweide projection. Since the map is more nearly circular than the Mollweide it makes smaller distance errors for points on opposite sides of the international date line in the Pacific. Also, the lengths of the different meridians are more nearly equal on the map. This has distance errors of 36.5%. For comparison, Figs. 1 and A2 show the Gott equal-area elliptical projection of the WMAP 3-year data and the planet Mars respectively.

We were interested to see if the Lambert equal-area azimuthal projection could be improved upon. Thus Gott and Mugnolo placed 3,000 particles down randomly on the sphere and mapped them onto the plane with the Lambert equal-area azimuthal projection. They then established a radial force between each pair of particles governed by a potential which is proportional to the square of the logarithmic distance error for that pair of particles on the map. Each particle is then allowed to move under the sum of the forces from the other particles in the planar map. This is an N -body problem in the plane. After one time step, their motion is stopped. The total potential energy of the system should be less than before. This is then repeated until the system settles into a relaxed distribution where the potential and therefore the rms logarithmic distance errors between pairs of points is in a local (and perhaps global) minimum. The 3,000 particles give 4,498,500 pairs of distances. The radial distribution of points (r as a function of latitude ϕ) can then be plotted. This makes a tight scatter diagram which can be approximated by the simple analytic formula:

$$r = \sin[0.446(\pi/2 - \phi)] \quad (\text{A3})$$

Figure A3. Map of the moon using the Gott-Mugnolo azimuthal projection. This has the smallest distance errors (34.1%) of any projection studied. Original imaging data come from the NASA's Clementine Satellite; the near face is in the center with the far side as an annulus surrounding it. The north and south poles are visible as places where the shadows are prominent, because the sun is always at low elevation there.

(The formula for the Lambert equal-area azimuthal is similar except 0.446 is replaced by $1/2$.) Thus our formulae for the (x, y) Cartesian coordinates on the Gott-Mugnolo azimuthal projection are:

$$\begin{aligned}x &= \cos \lambda \sin[0.446(\pi/2 - \phi)] \\ y &= \sin \lambda \sin[0.446(\pi/2 - \phi)].\end{aligned}\quad (\text{A4})$$

Checking with 30,000,000 random pairs, we find that this map projection has distance errors of only 34.1% which is the lowest of all the map projections we have studied. The WMAP 3-year data are shown in this map projection in Fig. 3, (a corresponding lunar map using this projection is shown in Fig. A3.) The value of the optimal constant 0.446 was then checked to an accuracy of two significant figures by varying this constant and minimizing the errors. Given the symmetry of the problem, it is perhaps not surprising that the best projection of the sphere for distance errors gives a map that is circular in shape. These techniques may find future applications for maps of the earth and of particular regions, as well as for the mapping of irregularly shaped asteroids.

This figure "fig1.jpg" is available in "jpg" format from:

<http://arxiv.org/ps/astro-ph/0610764v1>

This figure "fig2.jpg" is available in "jpg" format from:

<http://arxiv.org/ps/astro-ph/0610764v1>

This figure "figA2.jpg" is available in "jpg" format from:

<http://arxiv.org/ps/astro-ph/0610764v1>

This figure "fig3.jpg" is available in "jpg" format from:

<http://arxiv.org/ps/astro-ph/0610764v1>

This figure "figA3.jpg" is available in "jpg" format from:

<http://arxiv.org/ps/astro-ph/0610764v1>

This figure "fig10.jpg" is available in "jpg" format from:

<http://arxiv.org/ps/astro-ph/0610764v1>